Coulomb breakup reaction of loosely bound ^{17}F with dynamic polarization potentials

Kyoungsu Heo and Myung-Ki Cheoun
Department of Physics and Origin of Matter and Evolution of Galaxy (OMEG) Institute, Soongsil University, Seoul 06978, Korea

Ki-Seok Choi and K. S. Kim
School of Liberal Arts and Science, Korea Aerospace University, Koyang 10540, Korea

W. Y. So*
Department of Radiological Science, Kangwon National University at Dogye, Samcheok 25945, Korea

(Received 16 September 2021; accepted 21 December 2021; published 3 January 2022)

We investigate the elastic scattering, inelastic scattering, breakup reaction, and total fusion reactions of the $^{17}\mathrm{F} + ^{208}\mathrm{Pb}$ system using an optical model approach by including the dynamical polarization potential. In particular, we focus on the breakup reaction channels, whose effects on other reactions have been argued to be small. By exploiting two different potentials composed of a surface-type Woods-Saxon potential, which were obtained by a fitting analysis, and a Love-type optical potential, the breakup reaction cross sections are explained with other elastic and quasielastic scattering cross sections. For the breakup reaction at $E_{\mathrm{lab}} = 170$ MeV in the forward angle region, where only exclusive reaction data are known, inclusive breakup reaction data are deduced from available theoretical and experimental $E1$ strength values. We discuss the breakup reaction effects on the other nuclear reactions related to the ^{17}F projectile in detail.

DOI: 10.1103/PhysRevC.105.014601

I. INTRODUCTION

In general, the optical model (OM) is typically used to describe the elastic scattering data between projectiles and target nuclei in terms of one channel. According to this model, except for the elastic scattering channel described by the one channel, all other channels including the breakup reaction, the neutron and proton transfer reaction, and the fusion reaction are considered to be absorption channels. However, the OM has a disadvantage in that it cannot distinguish between direct and fusion reactions in the absorption channel. Consequently, an improved OM is required to explain fusion reaction from the view point of the direct reaction (DR) [1–8]. To this end, Udagawa *et al.* extended and developed the OM by decomposing the absorption reaction channel into DR and fusion reaction channels within the same framework [1–8]. This approach is known as the extended OM.

In order to apply the extended OM, the dynamic polarization potential (DPP) was used [9,10], which has a volume-type Woods-Saxon potential corresponding to the fusion part and a surface-derivative-type Woods-Saxon potential corresponding to the DR part. Then, the optimal parameters of the DPP were extracted, which simultaneously satisfied the elastic scattering, other DRs, and fusion cross sections, using χ^2 analysis. It was considered remarkable that the extended OM could well explain the nuclear reaction of not only tightly bound projectiles [3,6] but also weakly bound projectiles [7,8] on the heavy target nuclei.

However, in the case of weakly bound neutron-rich halo nuclei such as ^{6}He, ^{11}Li, and ^{11}Be, the simple extended OM described above cannot explain the experimental data of elastic and breakup reactions including the valence neutron(s) effect [11–14]. In general, these halo nuclei are composed of a charged core nucleus and one (or two) valence neutron(s). Therefore, owing to the Coulomb interaction generated by the target nucleus, the core nucleus acts on a repulsive force, but the valence neutron(s) does not act on any force. For this reason, the breakup reaction channels related to the $E1$ transition in the continuum state are easily opened by the Coulomb interaction. This phenomenon is called Coulomb dipole excitation (CDE) [15–17]. A new form of the DPP, such as the CDE and long-range nuclear (LRN) potentials, is required to describe the breakup reaction of the valence neutron(s) in neutron-rich halo nuclei. In our previous papers [18–23], we clarified the nuclear reaction of neutron-rich halo nuclei such as ^{6}He, ^{11}Li, and ^{11}Be using the extended OM including the CDE and LRN potentials.

One point to note is that the CDE potential can also be used to explain the inelastic scattering cross sections due to the first excited state associated with the $E1$ transition. Unlike ^{6}He or ^{11}Li nuclei, the other typical neutron-rich nucleus, ^{11}Be, has a low separation energy ($S_n = 504$ keV) and one excited state at an energy level ($E_x^{1\mathrm{st}} = 320$ keV) below the separation energy [24]. In our previous study [21], we investigated the contribution of the inelastic scattering channel to consider the first excited state related to the $E1$ transition for a $^{11}\mathrm{Be} + ^{197}\mathrm{Au}$

*wyso@kangwon.ac.kr

system below the Coulomb barrier energy, $E_{\rm c.m} = 30.1$ MeV. Our theoretical results could well explain the experimental data. Additionally, Coulomb excitation potentials related to the $E2$ transition, the $E3$ transition, and so on, may also exist. The DPP related to the $E2$ transition by Coulomb interaction is called the Coulomb quadrupole excitation (CQE) potential. One CQE potential was suggested by Love *et al.* [9] that was useful for taking into account the contribution of the inelastic scattering channel in the bound state to the elastic channel, or the breakup reaction channel in the continuum state to the elastic channel. Using Love's CQE potential considering the Coulomb excitation effect, the reduction in P_E, which is the ratio of the elastic scattering cross section to that of Rutherford scattering, has been well explained for the $^{12}\mathrm{C} + ^{184}\mathrm{W}$ system [9,25], the $^{18}\mathrm{O} + ^{184}\mathrm{W}$ system [9,25], and so on.

Until now, we have only investigated neutron-rich halo nuclei using the extended OM. However, recently, many interesting experiments have been reported for the scattering of light neutron-deficient (or proton-rich) nuclei projectiles on heavy target nuclei, such as the $^{17}\mathrm{F} + ^{208}\mathrm{Pb}$ system at $E_{\rm lab} = 86$ MeV [26], 90.4 MeV [27], 94.5 MeV [28], 98 MeV [27,29], 120 MeV [29], and 170 MeV [30,31]. Along with the data, many theoretical papers have analyzed the elastic (or quasielastic) scattering of $^{17}\mathrm{F}$ on the $^{208}\mathrm{Pb}$ target [28,32,33]. To this end, these papers have exploited the continuum-discretized coupled channel (CDCC) method. References [32,33] have calculated the elastic scattering cross sections with the CDCC formalism including folding potential and microscopic treatment for the projectile nucleus $^{17}\mathrm{F}$ at $E_{\rm lab} = 170$ MeV. In Ref. [28], also, they have reported additional experimental data of the quasielastic scattering at $E_{\rm lab} = 94.5$ MeV and theoretical analysis by the CDCC and coupled reaction channel (CRC) methods in which transfer channels of one or two nucleons are considered. Here we note that the CDCC calculations in these papers focused on the description of the elastic scattering channel.

Therefore, in this paper, we simultaneously calculate the angular distributions of $^{17}\mathrm{F}$ on $^{208}\mathrm{Pb}$ measured for elastic, inelastic, and breakup channels at $E_{\rm lab} = 98$, 120, and 170 MeV using the extended OM approach by considering the DPP in order to consider the elastic channels as well as other reaction channels. The reason behind choosing these three energies is that the quasielastic (QE; elastic + inelastic) scattering and the breakup reaction cross sections exist together [27,29]. A representative proton-rich nucleus $^{17}\mathrm{F}$ is assumed to have a core nucleus of $^{16}\mathrm{O}$ and one weakly bound valence proton. The separation energy of the valence proton for $^{17}\mathrm{F}$ (S_p) is approximately 600 keV, and there exists one excited state ($E_x^{\rm 1st} = 495$ keV), which is related to the $E2$ transition, below the separation energy [30]. This implies that the inelastic scattering and breakup reaction channels can be easily opened because the separation energy and the first excitation energy of the $^{17}\mathrm{F}$ projectile are smaller than 1 MeV. Therefore, when calculating the elastic scattering cross sections for the $^{17}\mathrm{F} + ^{208}\mathrm{Pb}$ system, the inelastic scattering and the breakup reaction channels must be considered together.

This paper is organized as follows. In Sec. II, we summarize the formalism of the OM and describe the optical potential used in the present study. In Sec. III, we investigate the elastic scattering, inelastic scattering, breakup reaction, and total fusion cross sections of the $^{17}\mathrm{F} + ^{208}\mathrm{Pb}$ system from a simultaneous χ^2 analysis using the DPPs. We then discuss the characteristics of proton-rich nuclei through the breakup reaction and extract the theoretical elastic scattering cross section using the inelastic scattering potential. Finally, we summarize our results and conclude our paper in Sec. IV.

II. FORMALISM

To simultaneously calculate the angular distributions of $^{17}\mathrm{F}$ on $^{208}\mathrm{Pb}$ measured for the elastic, inelastic, breakup, and total fusion channels in the scattering, we use the Schrödinger equation as follows [7,8,34]:

$$[E - T_l(r)]\chi_l^{(+)}(r) = U_{\rm OM}(r)\ \chi_l^{(+)}(r), \tag{1}$$

where $T_l(r)$ is a kinetic energy operator expressed as a function of the angular momentum l, and $\chi_l^{(+)}(r)$ is a distorted partial wave function. In Eq. (1), the OM potential $U_{\rm OM}(r)$ is composed of the real monopole Coulomb potential $V_{\rm C}(r)$, the real energy-independent bare potential $V_0(r)$, the imaginary inelastic scattering potential $W_{\rm inel.}(r)$, and the complex DPP $U_{\rm DPP}(r)$ as follows:

$$\begin{aligned} U_{\rm OM}(r) &= V_{\rm C}(r) - V_0(r) - W_{\rm inel.}(r) - U_{\rm DPP}(r) \\ &= V_{\rm C}(r) - V_0(r) - W_{\rm inel.}(r) - [V_{\rm DPP}(r) + iW_{\rm DPP}(r)]. \end{aligned} \tag{2}$$

In the OM, the real part is related to the elastic scattering channel and the imaginary part is related to other absorption channels. It should be noted that the energy-independent bare potential consists of three parts as follows: The first is the interaction between the core nucleus of $^{17}\mathrm{F}$ projectile ($^{16}\mathrm{O}$) and the target nucleus ($^{208}\mathrm{Pb}$). The second is the interaction between the valence proton and the target nucleus. The third is the interaction between the valence proton and the core nucleus. In principle, to obtain the bare potential of the $^{17}\mathrm{F} + ^{208}\mathrm{Pb}$ system, we have to extract each potential parameter by χ^2 fitting to the elastic scattering data for the $^{16}\mathrm{O} + ^{208}\mathrm{Pb}$ and $p + ^{208}\mathrm{Pb}$ systems and solving the bound state problem for the p-$^{16}\mathrm{O}$ interaction as followed in Refs. [12,14] for the $^{11}\mathrm{Li} + ^{208}\mathrm{Pb}$ and $^{11}\mathrm{Be} + ^{64}\mathrm{Zn}$ systems. In this work, however, we use a microscopic folding potential [35]:

$$V_0(r) = \int d\mathbf{r}_1 \int d\mathbf{r}_2 \rho_1(r_1)\rho_2(r_2) v_{NN}(r_{12} = |\mathbf{r} - \mathbf{r}_1 + \mathbf{r}_2|). \tag{3}$$

Here, v_{NN} is the M3Y interaction including the knock-on exchange effect [35,36] and is given as

$$v_{NN}(r) = 7999\frac{e^{-4r}}{4r} - 2134\frac{e^{-2.5r}}{2.5r} - 276\delta(r). \tag{4}$$

In Eq. (3), the nuclear matter distribution for the target nuclei, $\rho_1(r_1)$, is given in the Woods-Saxon form [37]:

$$\rho_1(r) = \rho_0 / \left[1 + \exp\left(\frac{r - c}{z}\right)\right], \tag{5}$$

with $\rho_0 = 0.164$ fm^{-3}, $c = 6.624$ fm, and $z = 0.549$ fm, while $\rho_2(r_2)$ is the nuclear matter distribution for the projectile

nucleus, which consists of a core nucleus (^{16}O) and a valence proton, as follows [36,38,39]:

$$\rho_2(r) = \rho_2^{^{16}\mathrm{O}}(r) + \rho_2^{p}(r), \tag{6}$$

with

$$\rho_2^{^{16}\mathrm{O}}(r) = 0.1317(1 + 0.6457r^2)\exp(-0.3228r^2), \tag{7}$$

and

$$\rho_2^{p}(r) = \left(\frac{3}{2\pi R_h^2}\right)^{\frac{3}{2}} \exp\left(-\frac{3r^2}{2R_h^2}\right), \quad \text{with } R_h = 3.78 \text{ fm}. \tag{8}$$

Here, we take the nuclear matter densities of the core nucleus and the valence proton from Refs. [36,38,39].

Next, we must determine the inelastic scattering potential $W_{\text{inel.}}(r)$ related to the $E2$ transition in order to consider the first excited state of the ^{17}F projectile as follows [9]:

$$W_{\text{inel.}}(r) = \begin{cases} -\left[1 - \frac{2}{7}\left(\frac{r_C}{r}\right)^2 - \frac{1}{21}\left(\frac{r_C}{r}\right)^4\right] K_C(r)\frac{W_P}{r^5} & \text{for } r \geqslant r_C, \\ -\frac{2}{3}K_C\,\frac{W_P r^4}{r_C^9} & \text{for } r < r_C, \end{cases} \tag{9}$$

with

$$K_C(r) = \left[1 - \frac{Z_1 Z_2 e^2}{r E_{\text{c.m.}}}\right]^{-1/2} \tag{10}$$

and

$$W_p = 0.01676\frac{\mu Z_i^2}{k} B(E2) g_2(\xi) \quad \text{for } i = 1 \text{ or } 2. \tag{11}$$

Note that in Ref. [9], K_C in Eq. (9) is replaced by the value of $\sqrt{10} \approx 3.16$ for $r < r_C$ because it diverges at $r = Z_1 Z_2 e^2/E_{\text{c.m}}$ in Eq. (10). In Eq. (11), μ is the reduced mass, k is the wave number defined by $\sqrt{2\mu E_{\text{c.m}}}/\hbar$, $B(E2)$ is the quadrupole electric transition strength, and $g_2(\xi)$ is an adiabaticity correction factor, which is a function of the adiabaticity parameter $\xi = a_0\varepsilon/\hbar v$, [9,15]. Here, a_0 is the distance of the closest approach in a head-on collision. More information on this potential can be found in Ref. [9]. It should be noted that the inelastic scattering potential $W_{\text{inel.}}(r)$ is not used for χ^2 fitting to determine the optimized parameters because χ^2 fitting for QE scattering cross-section data is performed in this work. Furthermore, this potential is used to predict the elastic and inelastic scattering cross sections and is discussed again in Sec. III.

Finally, we consider the DPP, $U_{\text{DPP}}(r)$, in Eq. (2). In general, the DPP consist of a real part $V_{\text{DPP}}(r)$ and an imaginary part $W_{\text{DPP}}(r)$. As mentioned earlier, because the valence proton in the ^{17}F nucleus is easily separated by the Coulomb and interacts with the target nucleus ^{208}Pb, the breakup reaction increases considerably. This interaction mainly occurs on the surface or at a distance farther than that because the valence proton of the projectile is primarily affected by the Coulomb interaction generated by the target nucleus. For this reason, we must introduce another surface-type Woods-Saxon potential to describe the interaction between them as follows:

$$U^{\text{BU}}(r) = 4a_i^{\text{BU}}(V^{\text{BU}} + iW^{\text{BU}})\frac{d\left[1 + \exp\left(X_i^{\text{BU}}\right)\right]^{-1}}{dR_i^{\text{BU}}}, \quad i = 0 \text{ and } W, \tag{12}$$

where $X_i^{\text{BU}} = (r - R_i^{\text{BU}})/a_i^{\text{BU}}$ with $R_i^{\text{BU}} = r_i^{\text{BU}}\,(A_1^{1/3} + A_2^{1/3})$. The subscript "BU" refers to the breakup reaction. Moreover, as an additional DPP in Eq. (2), we have to consider the total fusion reaction between the projectile and the target nucleus. This is because the nuclear fusion reaction takes place inside the target nucleus mainly when the projectile passing through the Coulomb barrier fuses with the target nucleus. Thus, a volume-type Woods-Saxon potential is adopted as follows:

$$U^{\text{TF}}(r) = (V^{\text{TF}} + iW^{\text{TF}})\left[1 + \exp\left(X_i^{\text{TF}}\right)\right]^{-1}, \quad i = 0 \text{ and } W \tag{13}$$

where $X_i^{\text{TF}} = (r - R_i^{\text{TF}})/a_i^{\text{TF}}$ with $R_i^{\text{TF}} = r_i^{\text{TF}}\,(A_1^{1/3} + A_2^{1/3})$. The subscript "TF" refers to the total fusion reaction. Finally, using these BU and TF potentials, the DPP can be expressed as follows:

$$\begin{aligned} U_{\text{DPP}}(r) &= U^{\text{BU}}(r) + U^{\text{TF}}(r) \\ &= [V^{\text{BU}}(r) + iW^{\text{BU}}(r)] + [V^{\text{TF}}(r) + iW^{\text{TF}}(r)]. \end{aligned} \tag{14}$$

III. RESULTS

A. Simultaneous χ^2 analysis

To obtain the optimized parameter sets for the BU and TF potentials in our calculations, we perform simultaneous χ^2 fitting for the experimental QE, breakup reaction, and total fusion cross-section data using the four adjustable parameters (V^{BU}, W^{BU}, V^{TF}, and W^{TF}) in Eq. (14). The extracted parameter sets are listed in Table I. In this work, we assume that the real and imaginary parts of the radius and the diffuseness ($a_0^{\text{BU}} = a_W^{\text{BU}}$, $r_0^{\text{BU}} = r_W^{\text{BU}}$, $a_0^{\text{TF}} = a_W^{\text{TF}}$, $r_0^{\text{TF}} = r_W^{\text{TF}}$) are fixed to be the same as each other. As indicated in Table I, after χ^2 fitting, the same value for all incident energies was obtained for three parameters ($r_0^{\text{BU}} = r_W^{\text{BU}}$, $a_0^{\text{TF}} = a_W^{\text{TF}}$, $r_0^{\text{TF}} = r_W^{\text{TF}}$); however, a value dependent on the energy was obtained for the diffuseness parameter for the TF potential, $a_0^{\text{BU}} = a_W^{\text{BU}}$. Details on the last three rows of the table are provided in Sec. III C.

Here we note that the difference between the χ^2 values at $E_{\text{lab}} = 98$ and 170 MeV amounts to dozens of times. This is because of the different error bars for the experimental elastic scattering data at the two incident energies. In practice, the related error bars are approximately 10% for the case of $E_{\text{lab}} = 98$ MeV and 1% for $E_{\text{lab}} = 170$ MeV, respectively, at forward angles. As a result, the χ^2 value defined as

$$\chi^2 = \sum_i^N \left(\frac{\sigma_{\text{th.}} - \sigma_{\text{expt.}}}{\Delta\sigma_{\text{expt.}}}\right)^2 \Big/ N \tag{15}$$

at $E_{\text{lab}} = 170$ MeV becomes larger than that at $E_{\text{lab}} = 98$ MeV. Here $\sigma_{\text{th.}}$, $\sigma_{\text{expt.}}$, $\Delta\sigma_{\text{expt.}}$, and N are the cross sections of the theoretical calculation, the experimental data, the error bar of the experimental data, and the number of data,

TABLE I. Optimized parameter sets of the DPPs for the $^{17}\mathrm{F}+^{208}\mathrm{Pb}$ system. $r_i = R_i/(A_1^{1/3}+A_2^{1/3})$ with $i = 0$ and W. Subscripts 0 and W denote the real and imaginary parts, respectively. The last three rows are the optimized parameter sets obtained from the simultaneous χ^2 fitting considering the Coulomb dipole excitation (CDE) potential of Eq. (19) for $E_{\mathrm{lab}} = 170$ MeV.

E_{lab} (MeV)	Set	V^{BU} (MeV)	W^{BU} (MeV)	$a_0^{\mathrm{BU}} = a_W^{\mathrm{BU}}$ (fm)	$r_0^{\mathrm{BU}} = r_W^{\mathrm{BU}}$ (fm)	V^{TF} (MeV)	W^{TF} (MeV)	$a_0^{\mathrm{TF}} = a_W^{\mathrm{TF}}$ (fm)	$r_0^{\mathrm{TF}} = r_W^{\mathrm{TF}}$ (fm)	χ^2
98		−0.70	0.073	0.343	1.64	−18.79	21.87	0.55	1.20	0.83
120		0.08	0.060	0.748	1.64	−9.46	99.94	0.55	1.20	5.16
170		0.13	0.041	0.651	1.64	−7.89	61.18	0.55	1.20	31.91
170	(A)	0.38	0.036	0.624	1.60	−13.11	40.54	0.55	1.20	40.43
170	(B)	0.39	0.018	0.569	1.62	−11.19	40.43	0.55	1.20	43.76
170	(C)	0.40	0.019	0.585	1.62	−11.30	39.96	0.55	1.20	43.57

respectively. The other point is that the V^{BU} and W^{BU} values in Table I are so small compared to others. This results from the fact that the breakup reaction cross sections are very small compared to the total reaction ones as shown in Table II and Fig. 3. To show that the parameters V^{BU} and W^{BU} we obtained are the most optimized values, we examine the alteration of the χ^2 values by changing the two parameters little by little after fixing the other parameters listed in Table I. Figure 1 shows the alteration of the χ^2 values according to the change of two parameters at $E_{\mathrm{lab}} = 98$ and 170 MeV, respectively. One can notice that, from the smallest χ^2 value by the two parameters [for example, $(V^{\mathrm{BU}}, W^{\mathrm{BU}}) = (-0.70, 0.073)$ for $E_{\mathrm{lab}} = 98$ MeV and (0.13, 0.041) for $E_{\mathrm{lab}} = 170$ MeV], the χ^2 value increases rapidly even if its value changes a little bit. In particular, this trend is salient by the change of W^{BU} rather than by the change of V^{BU}. This shows clearly that both parameters are optimized in the present χ^2 fitting to the available data.

It should be noted that, in this calculation, we use the QE scattering data instead of the elastic scattering data because there are currently no elastic scattering data available. To obtain the theoretical QE scattering cross sections, we perform χ^2 fitting using the experimental QE scattering data without the inelastic scattering potential, $W_{\mathrm{inel.}}(r)$, corresponding to the inelastic scattering channel in Eq. (2). Then, we extract the theoretical elastic scattering cross sections by subtracting the contribution from the inelastic scattering potential without additional χ^2 fitting. More details are provided in Sec. III B. By using these extracted optimal parameter sets, we then calculate the angular distributions of the elastic, QE scattering, and breakup reaction cross sections as well as the total fusion ones as a function of $E_{\mathrm{c.m.}}$. Finally, we plot them as shown in Figs. 2 and 3.

B. Elastic, inelastic, and quasielastic cross sections

As described in Sec. III A, we performed χ^2 fitting for the QE scattering cross sections, the theoretical results for which are plotted as solid black lines in Fig. 2(a) and are compared with the experimental data, represented using solid red circles. As shown in Fig. 2(a), the theoretical calculations for the QE scattering cross sections match well with the experimental data.

To extract the elastic scattering cross sections, we then need to perform a new calculation, subtracting the contribution from the inelastic scattering potential without additional χ^2 fitting. To do this, we utilize the inelastic scattering potential expressed using Eqs. (9)–(11) with $B(E2) = 21.64\ e^2\ \mathrm{fm}^4$ [40]. As a result, we can predict the theoretical calculations for the elastic scattering cross sections, denoted as the dashed blue lines in Fig. 2(a). However, the difference between the elastic and the QE scattering cross sections is indiscernible. Therefore, to investigate the contribution of the inelastic scattering cross section, we plot the ratio of the inelastic scattering

TABLE II. Inelastic, breakup, total fusion, and total reaction cross sections. Here, $\sigma_{\mathrm{R}}^{\mathrm{QE}}$ is extracted from the χ^2 fitting for the experimental quasielastic scattering cross-section data. σ_{R} is the summation of $\sigma_{\mathrm{R}}^{\mathrm{QE}}$ and the inelastic scattering cross sections $\sigma_{\mathrm{inel.}}$, which are obtained from the inelastic scattering potential using Eqs. (9), (10), and (11). The results of sets (A), (B), and (C) at $E_{\mathrm{lab}} = 170$ MeV are obtained by using the optimized parameter sets in Table I.

Energy (MeV)	Set		$\sigma_{\mathrm{Inel.}}$ (mb)	σ_{BU} (mb)	σ_{CDE} (mb)	σ_{TF} (mb)	$\sigma_{\mathrm{R}}^{\mathrm{QE}}$ (mb)	σ_{R} (mb)
98		Our result	126	75	–	279	354	480
98		Expt.	–	68 ± 5 [29]	–	317 ± 64 [41]	–	–
120		Our result	97	145	–	1330	1475	1572
120		Expt.	–	125 ± 7 [29]	–	–	–	–
170		Our result	74	95	–	2254	2349	2423
170	(A)	Our result	80	76	22	2174	2228	2308
170	(B)	Our result	80	35	106	2168	2309	2389
170	(C)	Our result	80	39	119	2166	2324	2404
170		Expt.	–	104 ± 10 [30]	–	–	–	–

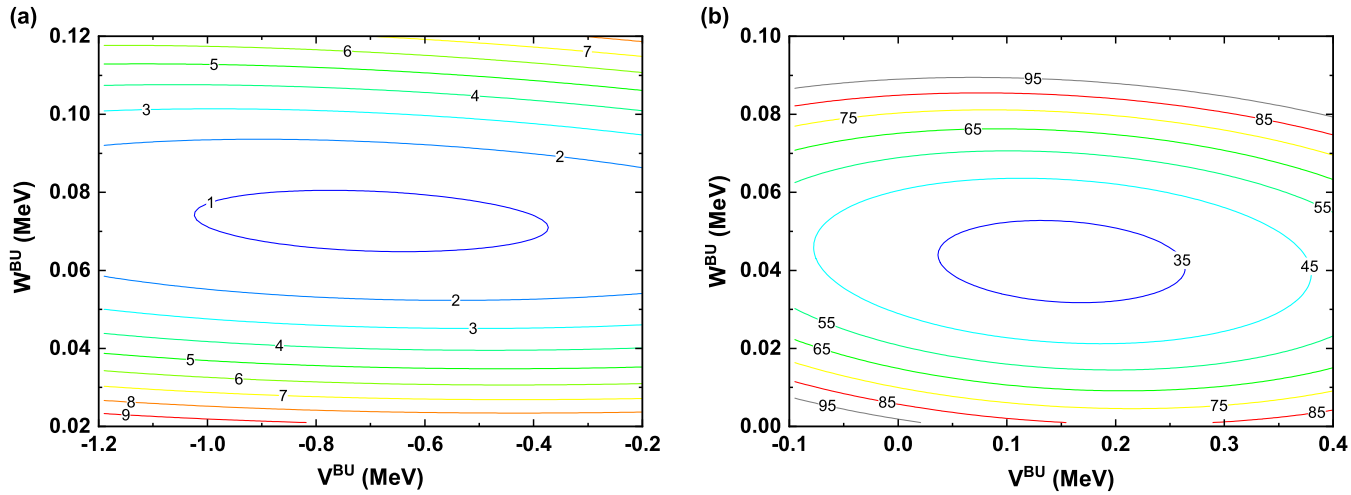

FIG. 1. The alteration of the χ^2 values due to the change of the real and imaginary depth parameters, V^{BU} and W^{BU}, for the surface-type Woods-Saxon potential in Eq. (12) for (a) $E_{\mathrm{lab}} = 98$ MeV and (b) $E_{\mathrm{lab}} = 170$ MeV.

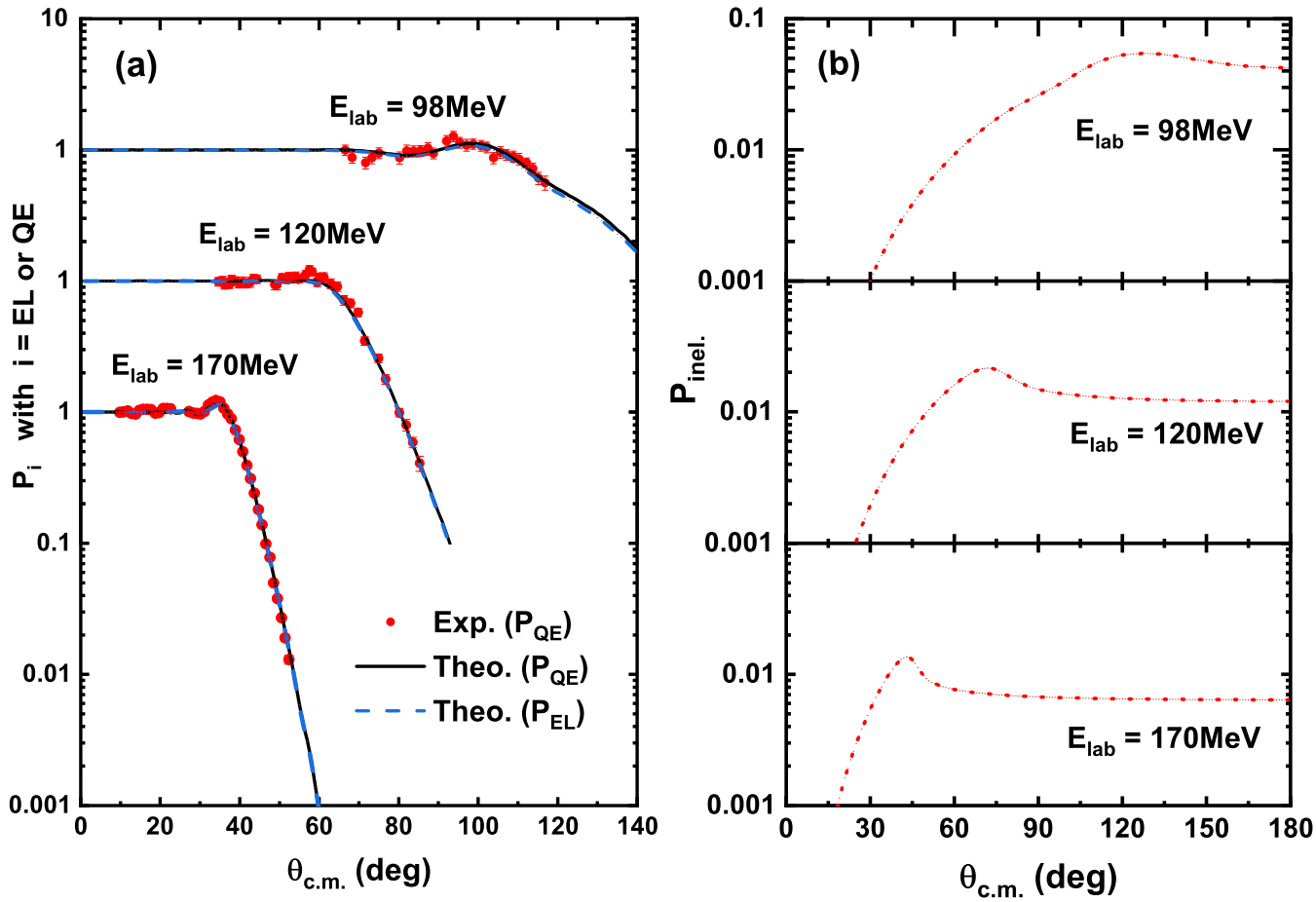

FIG. 2. Ratio $P_i = \sigma_i/\sigma_{\mathrm{RU}}$ with $i =$ elastic (EL), quasielastic (QE), and inelastic (inel.) for the $^{17}\mathrm{F} + ^{208}\mathrm{Pb}$ system. Here, σ_{EL}, σ_{QE}, $\sigma_{\mathrm{inel.}}$, and σ_{RU} are the elastic, quasielastic, inelastic, and Rutherford cross sections, respectively. In panel (a), the dashed blue and solid black lines represent the theoretical ratios P_{EL} and P_{QE}, respectively. Red circles denote the experimental P_{QE} data from Refs. [27,29,30] for the $^{17}\mathrm{F} + ^{208}\mathrm{Pb}$ system. In panel (b), the dotted red lines represent the theoretical ratio $P_{\mathrm{inel.}}$.

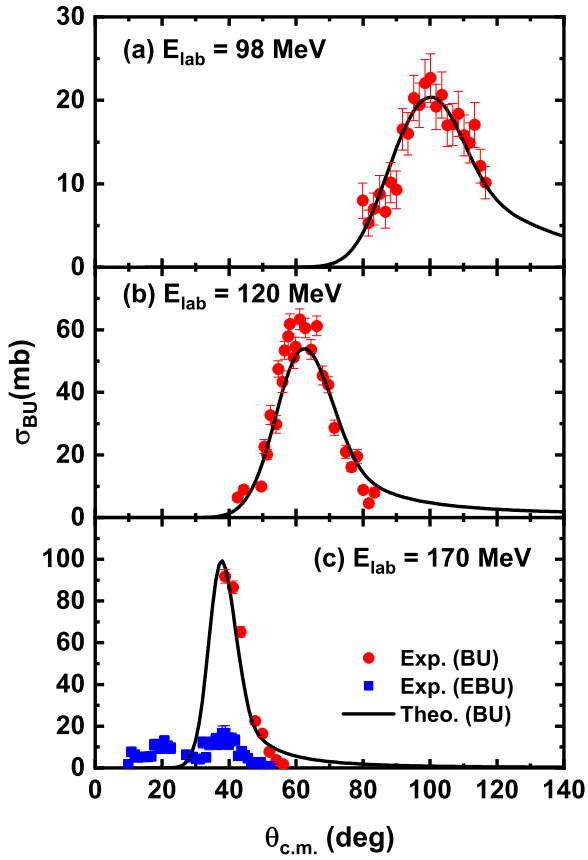

FIG. 3. Angular distribution of the breakup reaction cross sections for the $^{17}\mathrm{F}+^{208}\mathrm{Pb}$ system at $E_{\mathrm{lab}} = 98$, 120, and 170 MeV. The black solid lines represent the theoretically calculated angular distribution of the breakup reaction cross sections obtained from the simultaneous χ^2 analysis. Red solid circles and blue solid squares with error bars denote the experimental inclusive and exclusive breakup reaction cross-section data for the $^{17}\mathrm{F}+^{208}\mathrm{Pb}$ system, taken from Refs. [29,30] and Ref. [31], respectively.

cross sections to the Rutherford cross sections, denoted as $P_{\mathrm{inel.}}$ in Fig. 2(b). It can be seen that $P_{\mathrm{inel.}}$ lies below 0.1 at all incident energies. This implies that the inelastic scattering cross sections, which is the difference between QE and elastic scattering cross sections, is relatively small compared to the total fusion cross sections, as indicated in Table II, which lists the total inelastic scattering cross-section values as well as the breakup, total fusion, and total reaction cross-section values for each incident energy. Interestingly, the contribution of the inelastic scattering cross sections to the total reaction tends to decrease as the incident energy of the projectile increases.

C. Breakup and total fusion cross sections

From the simultaneous χ^2 analysis, we finally calculate the breakup reaction and total fusion cross sections. As indicated in Fig. 3, we compared experimental data (red solid circles) with theoretical calculations (black solid lines) for the differential inclusive breakup reaction cross sections. For reference, we provide the formula for the differential cross sections for each reaction channel adopted in our previous papers [6,20–22]:

$$\frac{d\sigma_i}{d\Omega} = \frac{ka_0}{16\pi}\frac{1}{\cos\left(\frac{\theta_{\mathrm{c.m.}}}{2}\right)\sin^3\left(\frac{\theta_{\mathrm{c.m.}}}{2}\right)}\sum_l \frac{\pi}{k}(2l+1)\,T_{i;l},$$
$$i = \text{inel., BU, CDE, and TF,} \tag{16}$$

with

$$T_{i;l} = \frac{8}{\hbar v}\int_0^\infty |\chi_l^+(r)|^2\, W_i(r)dr. \tag{17}$$

The imaginary potential type of each reaction channel in Eq. (17) is given in Eqs. (9), (12), (13), and (19), respectively. Note that the relative angular momentum l is defined by $l = \frac{ka_0}{2}\cot(\frac{\theta_{\mathrm{c.m.}}}{2})$ as a function of $\theta_{\mathrm{c.m.}}$. Also, from the integral over the scattering angle $\theta_{\mathrm{c.m.}}$, we can obtain the total cross section by each reaction channel listed in Table II using the following formula:

$$\sigma_i = \sum_l \frac{\pi}{k^2}(2l+1)\,T_{i;l}. \tag{18}$$

Our theoretical results reproduce the experimental data relatively well. However, as shown in Fig. 3(c), in addition to the inclusive BU reaction, experimental exclusive breakup (EBU) cross section data are also present at forward angles ($10^\circ \leqslant \theta_{\mathrm{c.m.}} \leqslant 50^\circ$) for $E_{\mathrm{lab}} = 170$ MeV. It is thought that there should exist some contributions from the inclusive cross sections around the forward region with $\theta_{\mathrm{c.m.}} \leqslant 30^\circ$. This may imply that an additional potential is needed to properly include the BU reaction at forward angles (or in long-range regions).

Therefore, in the following, we discuss how to include feasible inclusive breakup reaction contributions expected from the $B(E1)$ strength distribution around low-energy excited regions of $^{17}\mathrm{F}$. Hereafter, we deduce the BU cross sections expected to stem from those $E1$ transitions using the following CDE potential:

$$U_{\mathrm{CDE}}^{\mathrm{BU}}(r) = \frac{4\pi}{9}\frac{Z_t^2e^2}{\hbar v}\frac{1}{(r-a_0)^2 r}\int_{\varepsilon_b}^\infty d\varepsilon\frac{dB(E1)}{d\varepsilon}$$
$$\times\left[g\left(\frac{r}{a_0}-1,\xi\right)+if\left(\frac{r}{a_0}-1,\xi\right)\right], \tag{19}$$

with

$$f\left(\frac{r}{a_0}-1,\xi\right) = 4\xi^2\left(\frac{r}{a_0}-1\right)^2\exp(-\pi\xi)K''_{2i\xi}\left[2\xi\left(\frac{r}{a_0}-1\right)\right],$$

where Z_t is the charge number of the target nucleus and K'' is the second derivative of the modified Bessel function. The $g(\frac{r}{a_0}-1,\xi)$ function in Eq. (19) is the real part of the CDE potential, which is extracted from the dispersion relation [15] and given by

$$g\left(\frac{r}{a_0}-1,\xi\right) = \frac{P}{\pi}\int_{-\infty}^\infty \frac{f\left(\frac{r}{a_0}-1,\xi\right)}{\xi-\xi'}d\xi'. \tag{20}$$

First, we look up available experimental $B(E1)$ values. According to ENSDF data [40], there are $J^\pi = 1/2^-$ ($E_x = 3.104$ MeV) and $J^\pi = 5/2^-$ ($E_x = 3.857$ MeV) states with $B(E1)$ values of 0.001 53 and 0.004 38 W.u., respectively.

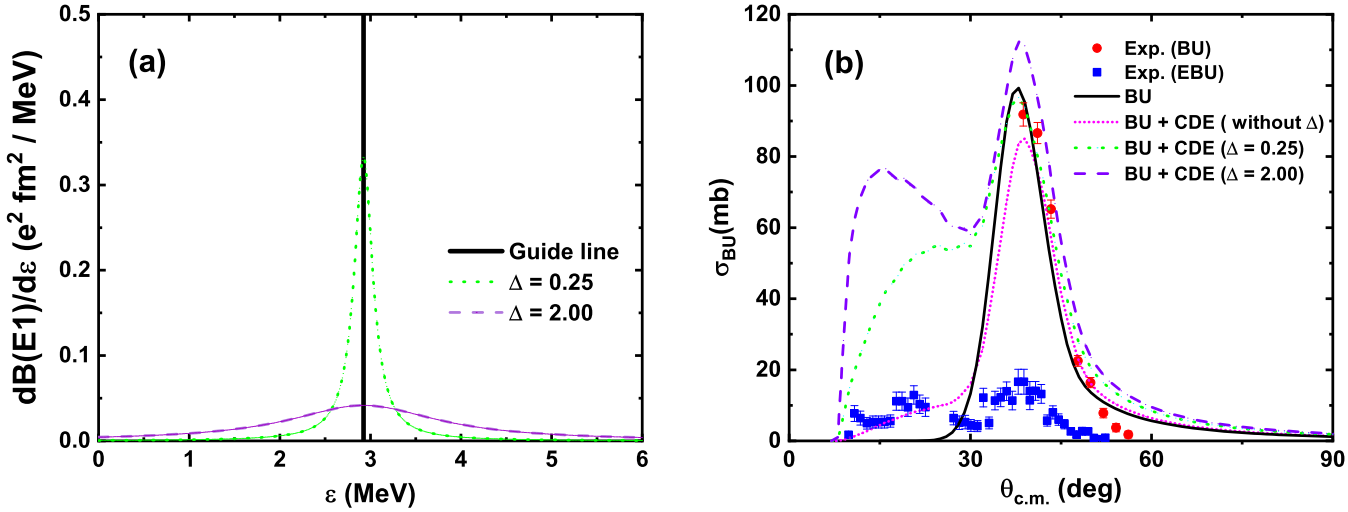

FIG. 4. (a) Coulomb strength distributions $dB(E1)/d\varepsilon$ as a function of Δ value for $B(E1) = 0.13\ e^2\ \mathrm{fm}^2$ at $\varepsilon = 2.92$ MeV. The solid black line is a guide line corresponding to $\varepsilon = 2.92$ MeV. (b) Angular distributions of the breakup reaction cross sections obtained by considering the CDE potential for the $^{17}\mathrm{F} + ^{208}\mathrm{Pb}$ system at $E_{\mathrm{lab}} = 170$ MeV. Experimental data are the same as those in Fig. 3(c). More details are provided in the text.

Here, E_x is the excitation energy, and W.u. is the abbreviation of the Weisskopf unit. In our calculations, however, we use only the experimental $B(E1) = 0.001\,53$ W.u. corresponding to the lowest excited state, $J^\pi = 1/2^-$ ($E_x = 3.104$ MeV), above the separation energy to extract the BU cross sections.

In order to investigate the BU cross sections obtained from the experimental $E1$ strength distribution, we reattempt to perform a simultaneous χ^2 analysis including the CDE potential of Eq. (19). In this calculation, we assume that the real and imaginary parts of the radius and the diffuseness ($a_0^{\mathrm{TF}} = a_W^{\mathrm{TF}}$, $r_0^{\mathrm{TF}} = r_W^{\mathrm{TF}}$) in the TF potential are fixed to be the same as each other. Then, we perform a simultaneous χ^2 analysis using six adjustable parameters (V^{BU}, W^{BU}, V^{TF}, W^{TF}, $a_0^{\mathrm{BU}} = a_W^{\mathrm{BU}}$, and $r_0^{\mathrm{BU}} = r_W^{\mathrm{BU}}$). Nevertheless, as the experimental $B(E1)$ value used is too small, the angular distribution of the BU cross sections is very insignificant. Therefore, we do not discuss these results by the experimental $B(E1)$ value any further in this paper.

Recently, De Gregorio *et al.* [42] illustrated the theoretical $B(E1)$ strength distribution in the low-energy region owing to the single-particle characters below the pygmy dipole resonance region, which are $B(E1) = 0.13\ e^2\ \mathrm{fm}^2$ at $E_x = 2.92$ MeV and $B(E1) = 0.22\ e^2\ \mathrm{fm}^2$ at $E_x = 6.49$ MeV. These values are much larger than the experimental ones. In Eq. (19), we employ the Coulomb strength distribution $dB(E1)/d\varepsilon$ proposed in Ref. [43] using the Lorentz function with the Lorentzian width Δ,

$$\frac{dB(E1)}{d\varepsilon} = \frac{1}{2\pi}\Sigma_n \frac{\Delta}{\left(\varepsilon - E_x^n\right)^2 + \left(\frac{1}{2}\Delta\right)^2} B(E1). \qquad (21)$$

Here, for $B(E1)$, we take the lowest peak [$B(E1) = 0.13\ e^2\ \mathrm{fm}^2$ at $E_x = 2.92$ MeV] because we are considering the energy region near the Coulomb barrier. E_x^n is the nth excitation energy. We perform simultaneous χ^2 analysis again in the same way as that using the experimental $B(E1)$ value, by changing the Lorentzian width Δ values in Eq. (21). As a result, we obtain three optimized parameter sets at $E_{\mathrm{lab}} = 170$ MeV listed in the last three rows of Table I. Set (A) in Table I is obtained by using a theoretical $B(E1)$ value of $0.13\ e^2\ \mathrm{fm}^2$ without the Δ value. Sets (B) and (C) are obtained by using a theoretical $B(E1)$ value of $0.13\ e^2\ \mathrm{fm}^2$ with $\Delta = 0.25$ and 2.00, respectively. Using these parameters, we can also extract the inelastic, breakup, CDE, total fusion, and total reaction cross sections in sets (A), (B), and (C) of Table II. Note that the total BU cross sections are the sum of the BU and CDE ones ($\sigma_{\mathrm{BU}} + \sigma_{\mathrm{CDE}}$) in the case of sets (A), (B), and (C) of Table II.

Figure 4(a) shows the Coulomb strength distribution $dB(E1)/d\varepsilon$ as a function of the Δ value for $B(E1) = 0.13\ e^2\ \mathrm{fm}^2$ at $\varepsilon = 2.92$ MeV. The dotted green and dashed violet lines represent the Coulomb strength distributions with $\Delta = 0.25$ and 2.00, respectively. It can be seen that, as the Δ value increases, the height and the depth of the distribution decreases and spreads, respectively. The (total) BU cross sections obtained from the theoretical Coulomb strength distribution $dB(E1)/d\varepsilon$ are also presented in Fig. 4(b). The short-dotted magenta, dotted green, and dashed violet lines are the BU cross sections obtained by the BU + CDE potential without Δ and with Δ values of 0.25 and 2.00, respectively. One interesting point in Fig. 4 is that the contribution of the EBU cross sections at the forward angle ($\theta_{\mathrm{c.m.}} \leqslant 30^\circ$) cannot be reproduced using only the surface-type Woods-Saxon potential (black solid line), whereas that of the inclusive BU cross section at a forward angle can be provided by adding the CDE potential (short-dotted magenta, dotted green, and dashed violet lines). Therefore, from Fig. 4(b), it can be seen that the contribution of the CDE potential in any form is required to account for feasible EBU cross sections at the forward angle.

We now discuss the BU effects on other reactions. Results are summarized for sets (A), (B), and (C) for $E_{\mathrm{lab}} = 170$ MeV

in Table II. Interestingly, despite considering the CDE potential, an increase in the (total) BU cross sections can be observed; however, the change in the total fusion cross sections is insignificant. This is attributed to the fact that the total fusion reaction occurs mainly when the incident nucleus and the target nucleus are close to each other; therefore, its cross section is not affected much because the CDE potential mainly acts in the long-range region. As a result, it can be seen that the total reaction cross sections also increase as the Δ value increases.

IV. CONCLUSIONS

In this study, we investigated the $^{17}\mathrm{F} + ^{208}\mathrm{Pb}$ system near and above the Coulomb barrier in order to evaluate the breakup reaction effects on other reactions relevant to the proton halo nucleus because the breakup reaction effects on neutron-halo or neutron-rich nuclei have already been clarified. To this end, we first calculated the Coulomb breakup cross sections for the $^{17}\mathrm{F} + ^{208}\mathrm{Pb}$ system for various energies and included the feasible inclusive BU process due to the CDE from the $B(E1)$ strength. The calculations were carried out using the OM, the potentials for which were extracted deliberately from existing data related to $^{17}\mathrm{F}$. Second, effects from the BU processes were quantitatively studied on other reactions related to $^{17}\mathrm{F}$. In conclusion, the breakup reactions on the $^{17}\mathrm{F} + ^{208}\mathrm{Pb}$ system may largely affect other nuclear reactions on the system rather than those expected in other previous discussions. However, additional breakup data for forward angles are required to draw a clearer conclusion on the breakup reaction effects on the halo nucleus $^{17}\mathrm{F}$.

ACKNOWLEDGMENTS

This work was supported by the National Research Foundation of Korea (Grants No. NRF-2021R1F1A1051935, No. NRF-2021R1F1A1046575, No. NRF-2020R1A2C3006177, No. NRF-2021R1A6A1A03043957, No. NRF-2017R1E1A1A01074023, and No. NRF-2013M7A1A1075764) and by MSIT (Grant No. 2018R1A5A1025563).

[1] T. Udagawa, B. T. Kim, and T. Tamura, Phys. Rev. C **32**, 124 (1985).
[2] T. Udagawa and T. Tamura, Phys. Rev. C **29**, 1922 (1984).
[3] S.-W. Hong, T. Udagawa, and T. Tamura, Nucl. Phys. A **491**, 492 (1989).
[4] T. Udagawa, T. Tamura, and B. T. Kim, Phys. Rev. C **39**, 1840 (1989).
[5] B. T. Kim, M. Naito, and T. Udagawa, Phys. Lett. B **237**, 19 (1990).
[6] B. T. Kim, W. Y. So, S. W. Hong, and T. Udagawa, Phys. Rev. C **65**, 044607 (2002).
[7] B. T. Kim, W. Y. So, S. W. Hong, and T. Udagawa, Phys. Rev. C **65**, 044616 (2002).
[8] W. Y. So, S. W. Hong, B. T. Kim, and T. Udagawa, Phys. Rev. C **69**, 064606 (2004).
[9] W. Love, T. Terasawa, and G. Satchler, Nucl. Phys. A **291**, 183 (1977).
[10] G. R. Satchler, M. A. Nagarajan, J. S. Lilley, and I. J. Thompson, Ann. Phys. (NY) **178**, 110 (1987).
[11] M. Cubero *et al.*, Phys. Rev. Lett. **109**, 262701 (2012).
[12] J. P. Fernández-García *et al.*, Phys. Rev. C **92**, 044608 (2015).
[13] A. Di Pietro *et al.*, Phys. Rev. Lett. **105**, 022701 (2010).
[14] A. Di Pietro *et al.*, Phys. Rev. C **85**, 054607 (2012).
[15] M. Andrés, J. Gómez-Camacho, and M. Nagarajan, Nucl. Phys. A **579**, 273 (1994).
[16] J. Gomez-Camacho, M. Andres, and M. Nagarajan, Nucl. Phys. A **580**, 156 (1994).
[17] M. Andrés, J. Christley, J. Gómez-Camacho, and M. Nagarajan, Nucl. Phys. A **612**, 82 (1997).
[18] W. Y. So, K. S. Kim, and M.-K. Cheoun, Phys. Rev. C **89**, 057601 (2014).
[19] W. Y. So, K. S. Kim, K. S. Choi, and M.-K. Cheoun, Phys. Rev. C **90**, 054615 (2014).
[20] W. Y. So, K. S. Kim, K. S. Choi, and M.-K. Cheoun, Phys. Rev. C **92**, 014627 (2015).
[21] W. Y. So, K. S. Choi, M.-K. Cheoun, and K. S. Kim, Phys. Rev. C **92**, 044618 (2015).
[22] W. Y. So, K. S. Choi, M.-K. Cheoun, and K. S. Kim, Phys. Rev. C **93**, 054624 (2016).
[23] K. Heo, M.-K. Cheoun, K.-S. Choi, K. S. Kim, and W. Y. So, Eur. Phys. J. A **56**, 42 (2020).
[24] I. Tanihata, H. Hamagaki, O. Hashimoto, Y. Shida, N. Yoshikawa, K. Sugimoto, O. Yamakawa, T. Kobayashi, and N. Takahashi, Phys. Rev. Lett. **55**, 2676 (1985).
[25] C. E. Thorn, M. J. LeVine, J. J. Kolata, C. Flaum, P. D. Bond, and J.-C. Sens, Phys. Rev. Lett. **38**, 384 (1977).
[26] C. Signorini, D. Pierroutsakou, B. Martin, M. Mazzocco, T. Glodariu, R. Bonetti, A. Guglielmetti, M. La Commara, M. Romoli, M. Sandoli, E. Vardaci, H. Esbensen, F. Farinon, P. Molini, C. Parascandolo, F. Soramel, S. Sidortchuk, and L. Stroe, Eur. Phys. J. A **44**, 63 (2010).
[27] M. Romoli *et al.*, Phys. Rev. C **69**, 064614 (2004).
[28] C. H. Rong *et al.*, Eur. Phys. J. A **57**, 143 (2021).
[29] J. F. Liang, J. R. Beene, A. Galindo-Uribarri, J. Gomez del Campo, C. J. Gross, P. A. Hausladen, P. E. Mueller, D. Shapira, D. W. Stracener, R. L. Varner, J. D. Bierman, H. Esbensen, and Y. Larochelle, Phys. Rev. C **67**, 044603 (2003).
[30] J. F. Liang, J. R. Beene, H. Esbensen, A. Galindo-Uribarri, J. Gomez del Campo, C. J. Gross, M. L. Halbert, P. E. Mueller, D. Shapira, D. W. Stracener, I. J. Thompson, and R. L. Varner, Phys. Rev. C **65**, 051603(R) (2002).
[31] J. F. Liang, J. R. Beene, A. L. Caraley, H. Esbensen, A. Galindo-Uribarri, C. J. Gross, P. E. Mueller, K. T. Schmitt, D. Shapira, D. W. Stracener, and R. L. Varner, Phys. Lett. B **681**, 22 (2009).
[32] J. Grineviciute and P. Descouvemont, Phys. Rev. C **90**, 034616 (2014).
[33] Ş. K. Çelik, İ. Boztosun, and M. Doğru, Few-Body Syst. **62**, 14 (2021).
[34] C. Mahaux, H. Ngo, and G. Satchler, Nucl. Phys. A **449**, 354 (1986).
[35] G. R. Satchler and W. G. Love, Phys. Rep. **55**, 183 (1979).
[36] M. El-Azab Farid and M. A. Hassanain, Nucl. Phys. A **678**, 39 (2000).

[37] C. W. De Jager, H. DeVries, and C. DeVries, At. Data Nucl. Data Tables **14**, 479 (1974).
[38] A. A. Ibraheem, A. S. Al-Hajjaji, and M. El-Azab Farid, Rev. Mex. Fis. **65**, 168 (2019).
[39] G. D. Alkhazov, A. V. Dobrovolsky, P. Egelhof, H. Geissel, H. Irnich, A. V. Khanzadeev, G. A. Korolev, A. A. Lobodenko, G. Munzenberg, M. Mutterer, S. R. Neumaier, W. Schwab, D. M. Seliverstov, T. Suzuki, and A. A. Vorobyov, Nucl. Phys. A **712**, 269 (2002).
[40] F. Ajzenberg-Selove, Nucl. Phys. A **375**, 1 (1982).
[41] K. E. Rehm, H. Esbensen, C. L. Jiang, B. B. Back, F. Borasi, B. Harss, R. V. F. Janssens, V. Nanal, J. Nolen, R. C. Pardo, M. Paul, P. Reiter, R. E. Segel, A. Sonzogni, J. Uusitalo, and A. H. Wuosmaa, Phys. Rev. Lett. **81**, 3341 (1998).
[42] G. De Gregorio, F. Knapp, N. Lo Iudice, and P. Vesely, Phys. Rev. C **95**, 034327 (2017).
[43] E. Guliyev, H. Quliyev, and A. A. Kuliev, J. Phys. G: Nucl. Part. Phys. **47**, 115107 (2020).